Raman scattering study of anharmonic phonon decay in InN

Núria Domènech-Amador, Ramon Cuscó, and Luis Artús
Institut Jaume Almera, Consell Superior d'Investigacions Científiques (CSIC), Lluís Solé i Sabarís s.n., 08028 Barcelona, Spain

Tomohiro Yamaguchi and Yasushi Nanishi
Faculty of Science and Engineering, Ritsumeikan University, 1-1-1 Noji-Higashi, Kusatsu, Shiga 525-8577, Japan
(Received 16 February 2011; published 17 June 2011)

We present Raman scattering measurements on wurtzite InN over a temperature range from 80 to 660 K. To investigate all phonon modes of the wurtzite structure, measurements were performed on *c* and *m* faces of high-quality InN epilayers. High-resolution measurements of the low-frequency E_2 mode reveal a slight anharmonic broadening of such a long-lived phonon due to up-conversion processes and a substantial contribution of background impurity broadening in the determination of its linewidth. An analysis of the anharmonicity and lifetimes of the InN phonons is carried out. Possible decay channels including up-conversion processes and four-phonon processes are discussed on the basis of density functional theory calculations.

DOI: 10.1103/PhysRevB.83.245203 PACS number(s): 78.30.Fs, 63.20.−e

I. INTRODUCTION

InN is attracting much interest since the revision of its fundamental bandgap energy from 1.9 to 0.7 eV,[1] which extends the emission range of the III-nitride system from deep-UV (AlN) down to the near-IR region.[2] In addition, InN exhibits unique transport properties, such as the smallest electron effective mass among the III-nitrides and very high saturation and peak drift velocities.[3] This makes InN a promising candidate for a wide range of devices spanning IR emitters, tandem solar cells,[4] and high-speed and high-frequency electronic devices.[5] The extended potential applications of InN have spurred in recent years the research on its optical and electrical properties.

Electron-phonon interaction is a key parameter in the design of high-speed devices as it governs the energy loss rate from electrons to the lattice via optical-phonon emission. For sufficiently long optical-phonon lifetimes, a large nonequilibrium phonon population can be maintained, which leads to phonon reabsorption and a significant reduction in the electron energy loss rate.[6] Such hot-phonon effects may severely degrade the performance of high-speed, high-field devices by causing a drift velocity saturation at high electric fields to values lower than predicted by theory.[7,8]

Carrier relaxation and hot-phonon effects are the subject of intense research in group III nitrides.[6,9–11] In polar semiconductors, carriers excited high in the conduction band relax toward their ground state mainly by Fröhlich interaction with the longitudinal optical (LO) phonons. The emitted phonons decay into other phonons, whose possible carrier absorption depends on their energy and polarity. Then, the total energy loss rate of carriers in polar semiconductors such as InN strongly depends on both the lifetimes and decay channels of the LO phonons. Thus, the dynamics of the phonon population affect the carrier–optical-phonon interaction which in turn is crucial for the understanding of novel wurtzite-based device heterostructures[12] and for the performance of high-speed devices.[8]

Moreover, the decay of LO zone-center phonons can give rise to a high population of large-wave-vector phonons, which may play a key role in ensuring momentum conservation in nonradiative Auger recombination processes. Auger recombination has been shown to be an important loss mechanism that contributes to the decrease of internal quantum efficiency of InGaN laser diodes at high drive currents.[13] Since for typical concentrations of injected carriers holes and electrons are confined in a small region around the Brillouin zone center, momentum conservation in intraband *eeh* Auger processes requires an additional wave vector to be transferred to the electron, and this can be supplied by a zone-edge phonon generated as a by-product of LO-phonon decay. The knowledge of phonon decay channels is therefore relevant to the evaluation of the efficiency of the Auger processes.

Due to the large mass difference between In and N, the phonon dispersion of InN exhibits a large gap between the upper-lying and lower-lying optical branches. This imposes restrictions onto the possible decay channels for optical phonons. Also, the E_2^{low} mode, which mainly involves In motion, displays a very low frequency in InN. Therefore, only acoustic branches with a low density of states (DOS) or up-conversion processes (i.e., decay into a higher-energy phonon by a phonon absorption) are available as decay channels and the E_2^{low} lifetime is expected to be very high. Recently, the E_2^{low} phonon lifetime has been measured in ZnO by means of impulsive stimulated Raman scattering experiments and it has been found to be longer than 200 ps at low temperatures. It has been suggested that such long-lived optical phonons could have applications in quantum cryptography and quantum computing.[14]

The LO-phonon dynamics can be investigated using both time-resolved[9,14,15] and frequency-resolved[16,17] techniques. In time-resolved Raman measurements, a nonequilibrium population of phonons is created by the cascade relaxation of photoexcited electrons through LO-phonon emission, and the decay rate of phonon population is measured. Large effective temperatures of the nonequillibrium LO phonons, typically in the 500–800 K range,[18] are reached in the pump-probe experiments. Furthermore, the hot-electron dynamics can affect the measured decay times. In fact, a large decrease of the LO-phonon lifetime has been found in InN at high densities of photoexcited electron-hole pairs.[18] A possible relaxation process that involves the emission of a plasma excitation[8] has been suggested to explain the carrier density dependence of the LO-phonon lifetime under such high excitation conditions.[18]

Alternative techniques for phonon lifetime measurements in the time domain are transient coherent ultrafast phonon spectroscopy (TCUPS)[15] and impulsive stimulated Raman scattering (ISRS).[14] In TCUPS the spectral interference of pairs of delayed pump pulses is analyzed as a function of the time delay to derive the phonon dephasing time. This technique overcomes the need for large phonon populations, and good agreement with conventional Raman results was reported for diamond.[15] In ISRS, the transmission modulation induced by the coherent phonons created by the pump beam is measured as a function of time using lock-in methods, and the time-domain oscillations are analyzed by means of Fourier transform and phase-correction algorithms to obtain the Raman line shape.[14] This has allowed the linewidth of the E_2^{low} mode of ZnO to be determined to an unprecedented accuracy [(0.0535 ± 0.002) cm^{-1}].[14]

Traditionally, phonon lifetimes have been measured in the frequency domain by means of high-resolution Raman scattering measurements.[16,17,19,20] Phonon lifetime is related to the linewidth of the Raman peak through the energy-time uncertainty relation. The temperature dependence of the phonon linewidth yields information about the phonon relaxation processes and is mainly governed by the occupation factors of the phonons involved. The temperature dependence of phonons in AlN and GaN has been widely studied by means of Raman scattering.[17,21–23] The knowledge of the temperature dependence of the phonon frequencies of GaN has been applied to determine the local temperature of a GaN diode as a function of the operating voltage.[24] While most of these studies adequately describe the temperature dependence of the phonons with a simple phenomenological model, the availability of *ab initio* calculations of the phonon density of states (PDOS) permits a more detailed evaluation of the anharmonic decay channels[11] as given by Cowley's perturbation theory.[25]

Because of the difficulties in obtaining high-quality samples, a limited number of phonon dynamics studies have been performed on InN. Early Raman studies of InN were reported in 1996 by Kwon *et al.*[26] using backscattering geometry and different polarization configurations, and an unambiguous identification of E_2^{high} and A_1(LO) phonon modes was given. Later, Davydov *et al.*[27] carried out Raman scattering measurements of InN in a variety of geometries, which allowed them to identify all the Raman active modes from their selection rules and to give a determination of the frequencies of all Raman-active phonons. First- and second-order Raman scattering experiments on hexagonal and cubic InN were reported by Kaczmarczyk *et al.*[28] In both works, phonon dispersion curves and PDOS obtained using phenomenological models were presented. These are consistent with the first-principles calculations reported later by Bungaro *et al.*[29] and with the *ab initio* results obtained in the present paper.

Raman scattering studies of the temperature dependence of phonons in InN were reported by Pomeroy *et al.*[30] and Pu *et al.*[31] In Ref. 31 the study was carried out over a limited temperature range (up to 443 K) on a metal-organic vapor-phase epitaxy (MOVPE) sample which showed disorder-related features in the Raman spectra and a rather broad E_2^{high} Raman peak. Both studies were restricted to the E_2^{high} and A_1(LO) phonon modes. Data analysis, carried out by fitting a simplified model, allowed them to conclude that the A_1(LO) mode decays asymmetrically into a high-energy and a low-energy phonon while the the E_2^{high} mainly decays through a four-phonon process, but the identification of the actual decay channels was not addressed.

In this paper, we have performed a detailed Raman scattering study of the temperature dependence of all the optical modes of InN. High-resolution measurements of the long-lived E_2^{low} mode are presented. The temperature dependence of the phonon linewidths and frequencies is discussed on the basis of Cowley's anharmonic theory and PDOS obtained from *ab initio* calculations. Besides confirming the dominant four-phonon process for the E_2^{high} mode decay, our analysis allows us to identify the most likely decay channels for the different modes. Up-conversion processes are seen to be predominant in the decay of the E_2^{low} mode. To explain the anharmonic decay of the LO modes at high temperatures a small contribution of higher-order processes is found to be necessary. The lifetime of the phonon modes is obtained from the width of the corresponding Raman peaks. The analysis of their temperature dependence allows us to estimate the anharmonic contribution and the background impurity contribution to the phonon decay rates.

II. EXPERIMENT

The experiments were performed on c and m faces of high-quality InN epilayers. The c-face sample was grown at 500 °C by plasma-assisted molecular beam-epitaxy (MBE) on GaN/sapphire templates, and the thickness of the film was 550 nm. The in-plane thermal expansion coefficient at 300 K of the InN is $\alpha_a = 3.6 \times 10^{-6}$ K^{-1},[32] which is a value similar to those corresponding to sapphire ($\alpha_a = 4.3 \times 10^{-6}$ K^{-1}) and to GaN ($\alpha_a = 3.8 \times 10^{-6}$ K^{-1}).[33,34] Thus, the biaxial strain is expected to be small in this sample. The m-face sample was grown on (100) γ-$LiAlO_2$, and the film thickness was 800 nm. The in-plane thermal expansion coefficient of this substrate at 300 K along the c axis is $\alpha_c = 14.9 \times 10^{-6}$ K^{-1},[35] which is considerably higher than the thermal expansion coefficient along the c axis found in InN for a similar temperature: $\alpha_c = 2.6 \times 10^{-6}$ K^{-1}.[32] Then, in this sample the temperature dependence of the phonon frequencies may be affected by the differential thermal expansion of the substrate. Electrical characterization of the samples was performed by standard Hall measurements, which showed that both samples display n-type conductivity. A free-electron density of 2.3×10^{18} cm^{-3} and a Hall mobility of $\mu_{\text{Hall}} = 1440$ cm^2 V^{-1} s^{-1} was measured in the c-face sample, whereas the m-face sample showed higher free-electron density (5×10^{19} cm^{-3}) and lower mobility ($\mu_{\text{Hall}} = 160$ cm^2 V^{-1} s^{-1}). While InN is known to have a surface electron accumulation layer, for the layer thickness and electron concentration of the layers studied here the surface sheet density is not expected to have a substantial effect on the Hall-derived electron density,[36] and we may consider that the Hall measurements basically reflect the n-type conductivity arising from the background donor impurities and threading dislocations.[36,37] Due to the difficulties in the growth of nonpolar faces, the density of dislocations

and defects is usually higher in m-face samples,[38] which results in an increment of electron density and a low electron mobility.

The Raman spectra were excited with the 514.5-nm line of an Ar^+ laser. Measurements in several scattering configurations were obtained using backscattering geometry on samples differently oriented. The m-face sample was used to obtain both the $x(zz)\bar{x}$ and the $x(zy)\bar{x}$ scattering configurations, while the c-face sample was used to measure the Raman spectra in the $z(--)\bar{z}$ configuration.

The scattered light was analyzed using a Jobin-Yvon T64000 triple spectrometer equipped with a LN_2-cooled charge-coupled device (CCD) detector. Raman spectra were obtained in the subtractive configuration of the spectrometer with 100-μm slits, corresponding to a spectral slit width of ≈ 2.2 cm^{-1}. The triple additive configuration with a 50-μm slit was utilized to obtain high-resolution spectra of the E_2^{low} mode. To minimize Rayleigh stray light, the intermediate slits of the spectrometer were set to 100 μm to allow only a narrow window of ≈ 30 cm^{-1} around the E_2^{low} frequency to reach the detector.

The Raman line shape measured in the experiments is the convolution of the natural Lorentzian line shape of the phonon with the Gaussian instrument broadening function. In order to separate both contributions, the instrument-broadening profile was checked in the different configurations by measuring the $\lambda = 546.07$ nm emission line of a Hg lamp, which was fitted by a Gaussian line shape with a full-width at half-maximum (FWHM) of $\Gamma_G = 2.2$ cm^{-1} ($\Gamma_G = 0.5$ cm^{-1} in the high-resolution triple additive configuration). Then, the phonon linewidths were evaluated using the Voigt profile approximation $\Gamma \approx 0.5346\Gamma_L + \sqrt{0.2166\Gamma_L^2 + \Gamma_G^2}$, where Γ is the FWHM of the measured Raman peak and Γ_L is the intrinsic FWHM of the phonon mode.[39] All the linewidth values given in this paper correspond to the intrinsic FWHM of the phonon modes.

A LN_2 cryostat was used to vary the sample temperature from 80 to 390 K. Within this temperature range, the spectra were acquired in macrocamera configuration. To extend the temperature range up to 660 K, we used a Linkam high-temperature stage, and the measurements were performed using a confocal microscope with a long-working-distance $\times 80$ objective protected by a cooling jacket. Very low excitation power was used to minimize local heating effects. Both sets of measurements yield consistent results in the overlapping temperature range between 290 and 390 K.

III. THEORETICAL FRAMEWORK

A. Anharmonic phonon decay

Lattice dynamics are usually described in the harmonic approximation, where the lattice potential is expanded up to quadratic terms in the atomic displacements. The actual lattice Hamiltonian contains, however, higher-order terms which give rise to the coupling of the harmonic eigenstates (*bare* phonons) leading to phonon decay and finite lifetime. The interaction between the harmonic eigenstates results in a renormalization of the *bare* phonon energies and lifetimes that can be described by the complex phonon self-energy $\Sigma(\omega) = \Delta(\omega) - i\Gamma(\omega)$. To the lowest order in perturbation theory, the cubic anharmonicity contribution to the imaginary part of the self-energy can be written as[16,25]

$$\Gamma^{(3)}(\omega) = \frac{18\pi}{\hbar^2}\sum_{\mathbf{q}j_1j_2}|V_3(\mathbf{q}j_1, -\mathbf{q}j_2)|^2 \times\{[n(\omega_1)+n(\omega_2)+1]\delta(\omega_1+\omega_2-\omega) +[n(\omega_2)-n(\omega_1)]\delta(\omega_1-\omega_2-\omega)\}, \quad (1)$$

where $V_3(\mathbf{q}j_1, -\mathbf{q}j_2)$ is the third-order coefficient in the expansion of the lattice potential in normal coordinates and $n(\omega)$ is the Bose–Einstein occupation factor. If we assume that the V_3 coefficients and the Bose–Einstein factors are constant over the small energy range considered, the imaginary part of the self-energy can be written as

$$\Gamma^{(3)}(\omega) = |V_3^+|^2[1+n(\omega_1^+)+n(\omega_2^+)]\rho^+(\omega) +|V_3^-|^2[n(\omega_2^-)-n(\omega_1^-)]\rho^-(\omega), \quad (2)$$

where $\rho^+(\omega)$ and $\rho^-(\omega)$ are, respectively, the two-phonon DOS for phonon sums and differences, and V_3^+ and V_3^- are the effective third-order anharmonic constants for decay into phonon sums and differences. If we further assume a constant two-phonon DOS the imaginary part of the self-energy and hence the phonon linewidth are simply proportional to the Bose–Einstein factors. Such a simple model has been widely used to analyze the temperature dependence of the the optical-phonon linewidths in a number of Raman scattering studies.[20,21,24,30,31,40–42] The crude Klemens's ansatz[40] (symmetrical decay into acoustic overtones) appears to work well for the Raman phonon line of diamond,[42] whereas more general, asymmetric decay channels have to be included to describe other semiconductors.[16,41] This is particularly important in group III nitrides, where the disparity in atomic masses opens a large phonon gap between optical and acoustic bands and therefore Klemens's decay channel is not possible.[43] While the simplified (constant DOS) model is appealing because it yields analytical expressions for the frequency and linewidth dependence on T, in some cases it misses important effects of the details of the phonon dispersion. An anomalous temperature dependence of phonon lifetimes and phonon line-shape asymmetries have been shown to be associated with features in the two-phonon DOS.[19,20,44–46] Unlike previous studies,[30] for the analysis of the temperature dependence of InN phonons we have taken into account the PDOS in the evaluation of the phonon linewidth.

As follows from Eqs. (1) and (2), to the lowest order (cubic anharmonicity terms) the phonon linewidth is governed by decay into pairs of phonons with opposite wave vectors and therefore it is proportional to the two-phonon DOS. Current density functional theory (DFT) codes such as ABINIT (Ref. 47) allow the PDOS to be calculated from first principles and thus permit the direct evaluation of Eq. (2). While the V_3^+, V_3^- anharmonic constants are related to the third derivative of the total energy with respect to the phonon displacement and can in principle be calculated also from first principles,[48] here we consider them as adjustable parameters that will be determined from the experimental data.

Higher-order decay processes into three phonons may be necessary to account for temperature dependence,

particularly at high temperatures. The contribution of quartic anharmonicity terms in the Hamiltonian was calculated by Balkanski *et al.*[41] Unfortunately, the sums over wave vectors of the three phonons involved are mathematically intractable, and the expressions given in Ref. 41 are difficult to evaluate explicitly. However, we can estimate the effect of the quartic anharmonicity term on the phonon linewidth by assuming that the most likely decay channels involve the decay into a zone-center phonon and a pair of opposite wave-vector phonons at the zone edges or at critical points of the phonon dispersion, where the PDOS is maximum. The specific phonon combinations for phonon decay that present the highest PDOS are selected for each phonon mode based on the calculated DOS. This simplification, together with the assumption of constant fourth-order anharmonic coefficients, reduces the quartic anharmonicity contribution to a term proportional to the two-phonon DOS,

$$\begin{aligned}\Gamma^{(4)}(\omega) \sim\ & |\tilde{V}_4^{+}|^2\{[n(\omega_1^+)+1][n(\omega_2^+)+1][n(\omega_3^+)+1]\\ & -n(\omega_1^+)n(\omega_2^+)n(\omega_3^+)\}\rho^+(\omega-\omega_1^+)\\ & +|\tilde{V}_4^{-}|^2\{[n(\omega_1^-)+1][n(\omega_2^-)+1]n(\omega_3^-)\\ & -n(\omega_1^-)n(\omega_2^-)[n(\omega_3^-)+1]\}\rho^-(\omega-\omega_1^-). \qquad (3)\end{aligned}$$

In Eq. (3), ω_1 is the frequency of the zone-center mode considered and ω_2, ω_3 are the frequencies of opposite wave-vector phonon modes satisfying energy conservation. It should be emphasized that $\tilde{V}_4{}^{+}$, $\tilde{V}_4{}^{-}$ are *effective* anharmonic constants for the channel considered, which include a DOS weight factor for the zone-center mode involved. In the present analysis, $\tilde{V}_4{}^{+}$, $\tilde{V}_4{}^{-}$ should be considered as empirical adjustable parameters whose direct comparison with V_3^+, V_3^- is not straightforward.

Since real and imaginary parts of the phonon self-energy are related by a Kramers–Kronig transformation, the corresponding real part of the self-energy, $\Delta(\omega)$, can be evaluated as

$$\Delta(\omega) = -\frac{2}{\pi}\mathcal{P}\int_0^\infty \frac{\omega'}{\omega'^2-\omega^2}\Gamma(\omega')d\omega'. \qquad (4)$$

This yields a frequency-dependent renormalization of the phonon energy, which has to be added to the frequency shift due to the thermal expansion of the lattice, Δ_0. This latter contribution can be written as[49]

$$\Delta_0 = -\omega_0\gamma\int_0^T [\alpha_c(T')+2\alpha_a(T')]dT', \qquad (5)$$

where α_c and α_a are the linear thermal expansion coefficients along directions parallel and perpendicular to the c axis, respectively,[50] and γ is the Grüneisen parameter of the phonon mode considered. Following Ref. 16, the frequency-independent fourth-order contribution is neglected in the analysis of our data. In fact, we do not aim to perform a precise calculation of the phonon frequencies in our InN epilayers as they may be significantly affected by residual strain and the differential thermal expansion of the substrate. These effects are difficult to evaluate due to the lack of a reliable set of parameters for InN. In addition, we consistently use in our model the phonon frequencies obtained from the DFT calculations, which may also contain deviations relative to the experimental phonon frequencies. Therefore, the calculations of the phonon frequencies vs. T are presented here only to illustrate the anharmonic shift that is predicted by the model using the anharmonic coefficients determined from the T dependence of the phonon linewidth. All the calculated frequency vs. T curves presented in this paper have been vertically shifted to match the experimental frequencies measured at low temperatures.

For small self-energy corrections compared with the Raman frequency, the line shape of the Raman peak is given by[16]

$$I(\omega) \propto \frac{\Gamma(\omega)}{[\omega_0+\Delta_0+\Delta(\omega)-\omega]^2+\Gamma(\omega)^2}. \qquad (6)$$

Note that in the case of a frequency-independent self-energy, the phonon line shape is Lorentzian with a FWHM equal to two times the imaginary part of the self-energy. If the self-energy depends on the frequency, the line shape can deviate from a Lorentzian line shape. The curves of phonon frequency and FWHM vs. T were obtained by determining for each temperature the peak frequency and FWHM of the Raman line shape numerically evaluated from Eq. (6).

B. Phonon dispersion: *Ab initio* calculations

The third- and fourth-order anharmonic contributions to the imaginary part of the phonon self-energy derived above are proportional to the PDOS for phonon sums and differences. Present-day *ab initio* codes allow phonon dispersion and DOS to be accurately calculated and therefore make possible the evaluation of Eqs. (2) and (3), taking fully into account the effect of the PDOS in the anharmonic decay rate. An *ab initio* calculation of the InN phonon dispersion was carried out using a plane-wave pseudopotential approach to the DFT as implemented in the ABINIT code package.[47] The calculations are performed in the local density approximation (LDA) using the Teter parametrization of the exchange-correlation[51] and Troullier-Martins pseudopotentials.[52] For the In pseudopotential the 4*d* electrons were included as valence states. An $8\times8\times4$ Monkhorst–Pack k-point sampling and a plane-wave basis set with an energy cutoff of 65 Ha were used in the calculations. A full structural relaxation of the wurtzite InN lattice was carried out and lattice parameters $a = 3.520$ Å, $c = 5.691$ Å were obtained, in good agreement with reported high-resolution x-ray diffraction values.[53] A good convergence of the phonon frequencies is achieved for all modes except for the longitudinal polar modes. According to previous results,[46] there is uncertainty in the values of the dielectric constant provided by the ABINIT code that may be related to the LDA gap problem and may affect the longitudinal phonon frequencies. In the case of ZnO, the code failed to predict the correct ordering of the A_1(LO) and E_1(LO) phonon frequencies.[46] In the case of InN, in addition to the incorrect frequency ordering, a spurious dispersion of the E_1(LO) mode is predicted along the Σ (Γ–M) and T (Γ–K) lines. However, since this paper is concerned with phonon decay channels, and hence with PDOS at frequencies lower than those of the E_1(LO) and A_1(LO) modes, the inadequacy of the calculated E_1(LO) and A_1(LO) frequencies does not affect our analysis. The dynamical matrix is obtained on a mesh of k points using the perturbation theory linear-response approach,[54,55] and the interatomic force constants are generated by a Fourier transformation. This

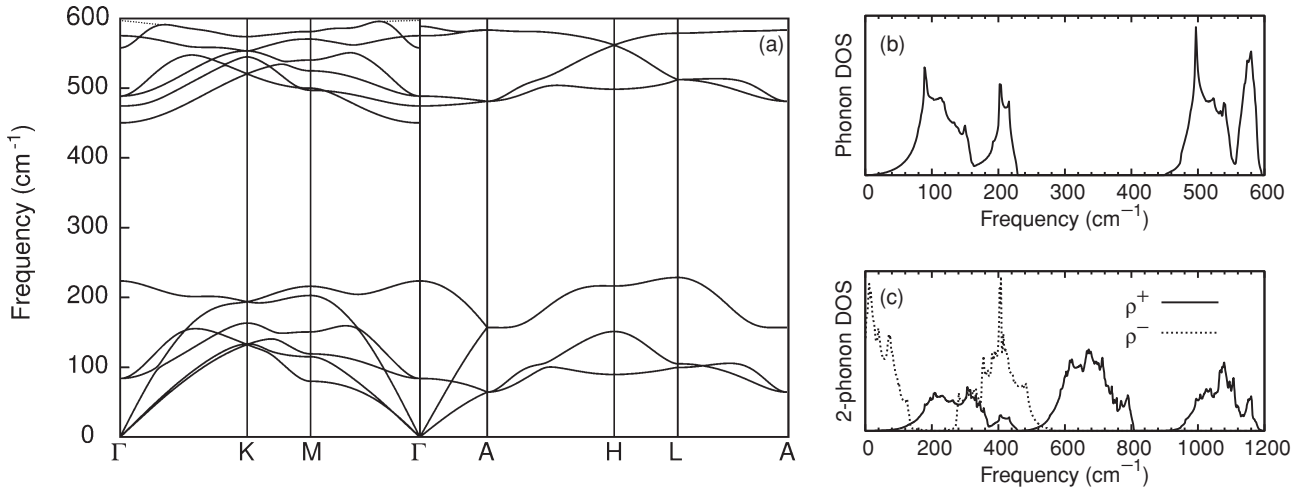

FIG. 1. (a) Phonon-dispersion relation of wurtzite InN. Dotted lines around Γ along Γ–M and Γ–K lines for the E_1(LO) mode correspond to data taken from Ref. 29. (b)PDOS. (c) Two-phonon DOS for sums (ρ^+) and differences (ρ^-) of opposite wave-vector phonons.

allows the dynamical matrices and phonon frequencies to be interpolated for arbitrary wave vectors, and thus the phonon dispersion over the whole Brillouin zone and the PDOS can obtained.

Figure 1 displays the calculated phonon dispersion along high-symmetry directions [Fig. 1(a)] as well as the PDOS [Fig. 1(b)] and the two-phonon DOS for sums (ρ^+) and differences (ρ^-) of phonons with opposite wave vectors [Fig. 1(c)]. The frequencies of the zone-center phonons are listed in Table I. As discussed above, the calculated E_1(LO) frequency exhibits a spurious dispersion near the zone center. The dotted lines in Fig. 1 represent the E_1(LO) dispersion calculated by Bungaro *et al.*[29] The deviation of the E_1(LO) phonon dispersion does not have any noticeable effect on the calculated PDOS, which agrees very well with the one reported in Ref. 29.

The PDOS [Fig. 1(b)] exhibits distinct maxima that can be traced to van Hove singularities in the phonon dispersion. In the acoustic-mode region, there are two sharp DOS maxima at 90 cm^{-1}, corresponding to transverse acoustic (TA) branches at H, and at 204 cm^{-1}, associated with longitudinal acoustic (LA) branches at M and along the Γ–K line. Other DOS maxima occur at 114 and 118 cm^{-1} [TA(M) and TA($L-A$)], 150 cm^{-1} [TA($M-K$)], 202 cm^{-1} [LA(M), LA(Γ $-$ K)], and 217 cm^{-1} [LA(M) and LA(H)]. In the optical-mode region, the sharp peak at 498 cm^{-1} corresponds to transverse optical (TO) modes at M and H, while the maxima at 523 cm^{-1} and 541 cm^{-1} are due to TO modes at M. The broader DOS band between 550 and 600 cm^{-1} reflects the longitudinal optical modes. It contains a sharp peak at 581 cm^{-1} associated with the flat dispersion along $L-A$ and $A-H$ and a secondary maximum at 575 cm^{-1} that corresponds to the zone-center B_1^{high}.

As can be seen in Fig. 1(c), $\rho^+(\omega)$ falls rapidly for frequencies $\lesssim$ 180 cm^{-1}. This rules out phonon decay into a sum of phonons for the E_2^{low} mode. By contrast, $\rho^-(\omega)$ displays high values in this region, providing likely decay channels for the E_2^{low} mode. Conversely, above $\sim$580 cm^{-1}, $\rho^-(\omega)$ vanishes whereas $\rho^+(\omega)$ steeply increases, and therefore the anharmonic decay of the LO modes is governed by phonon sums. It is worth noticing that there exists a gap in the two-phonon DOS between $\sim$500 and 550 cm^{-1} where both $\rho^+(\omega)$ and $\rho^-(\omega)$ are very low. This occurs in the frequency range of the E_2^{high} mode, and, as we shall see below, it has implications for the effective decay mechanism of the E_2^{high} mode.

The mode Grüneisen parameters γ required to evaluate Eq. (5) were also obtained from the *ab initio* calculations using the relation

$$\gamma = \frac{B}{\omega}\frac{\partial\omega}{\partial P}, \tag{7}$$

where $B = -V(\partial P/\partial V)$ is the bulk modulus. For a $6\times6\times4$ k-vector grid and cutoff energy of 60 Ha we obtain $B =$ 143 GPa and the values of Grüneisen parameters displayed in Table I. The Grüneisen parameter for the E_2^{low} mode is negative. As we shall discuss below, the soft-mode character of the E_2^{low} mode has a bearing on the temperature dependence of the E_2^{low} frequency, which turns out to exhibit a very small shift

TABLE I. Zone-center phonon frequencies and mode Grüneisen parameters for wurtzite InN calculated using the ABINIT code.

	E_2^{low}	B_1^{low}	A_1(TO)	E_1(TO)	E_2^{high}	B_1^{high}	A_1(LO)	E_1(LO)
ω	84.0	223.7	450.2	474.5	488.6	575.1	588.6	557.7
γ	−0.98	1.01	1.62	1.58	1.64	1.37	1.29	1.62

TABLE II. Symmetry-allowed Raman modes for the scattering configurations considered in this paper.

Scattering	Raman active modes				
configurations	E_2	A_1(LO)	A_1(TO)	E_1(LO)	E_1(TO)
$z(xx)\bar{z}$	A	A			
$z(xy)\bar{z}$	A				
$x(zz)\bar{x}$			A		
$x(yz)\bar{x}$					A

in the temperature range studied. The Grüneisen parameters of the E_2^{high} and A_1(LO) modes are in good agreement with those determined from hydrostatic pressure measurements assuming a bulk modulus of 146 GPa.[56]

IV. RESULTS AND DISCUSSION

A. First-order Raman scattering of InN

In this section we present the InN Raman spectra acquired at room temperature using different scattering configurations, and we compare the obtained results with those theoretically predicted and with previous studies.

Wurtzite-type InN belongs to the space group C_{6v}^4 with two formula units in the primitive cell. According to the factor group analysis, the zone-center optical-phonons belong to the following irreducible representations: $\Gamma_{opt} = A_1 + E_1 + 2E_2 + 2B_1$. The B_1 modes are silent, the A_1 and E_1 modes are polar modes and are both Raman and IR active, whereas the E_2 modes are nonpolar and Raman active only. Table II shows the selection rules for the Raman scattering under nonresonant conditions for the configurations used in this paper. All the Raman-active modes can be observed in backscattering geometry except the E_1(LO) mode. This mode is only dipole allowed in the $x(yz)y$ configuration. Owing to the strong optical absorption of InN, it is not possible to acquire the Raman spectra in such configuration. However, the E_1(LO) phonon mode is usually observed in the symmetry-forbidden $x(zz)\bar{x}$ configuration due to intraband Fröhlich interaction.[57]

Figure 2 shows first-order InN Raman spectra performed at room temperature in several backscattering configurations. The $z(--)\bar{z}$ spectrum exhibits three sharp peaks at 87, 494, and 584 cm^{-1}, corresponding to the E_2^{low}, E_2^{high}, and A_1(LO) modes, respectively. In addition to these modes there is a weak, broad feature around 180 cm^{-1} which does not correspond to any Raman-active mode. A peak in this region has been previously reported by different authors,[27,31,58,59] but its origin remains unclear. Pu *et al.*[31] assigned it to the silent mode B_1^{low}, but according to our theoretical calculations (see Sec. III B) the expected frequency for the B_1^{low} mode is 224 cm^{-1}, which is significantly higher than that of the Raman feature measured in the spectra. Kaczmarczyk *et al.*[58] attributed this feature to acoustic phonons around the A point. On the other hand, a recent study reports a similar peak around 170 cm^{-1} and assigns it to large-wave-vector LA phonons selectively excited by resonant Raman scattering.[59] Further work is required in order to ascertain the origin of this feature.

The $x(zz)\bar{x}$ and $x(yz)\bar{x}$ Raman spectra were recorded in backscattering geometry on an m-face sample. As can be seen in Table II, the dipole-allowed Raman modes in these configurations are A_1(TO) and E_1(TO), respectively. The $x(zz)\bar{x}$ spectrum displays two peaks at 452 and 597 cm^{-1} that can be clearly assigned to the A_1(TO) and to the symmetry-forbidden E_1(LO) phonon mode. As mentioned above, the latter is measured in forbidden backscattering geometries under near-resonant conditions on the m face due to intraband Fröhlich interaction.[27] The E_1(TO) phonon mode is detected at 478 cm^{-1} in the $x(yz)\bar{x}$ configuration. In this geometry we also observe residual Raman peaks related to A_1(TO), E_2^{high} and E_1(LO) phonon modes, which may arise from the relaxation of the selection rules in the lower quality m-face samples or from sample misalignment.

B. Anharmonic phonon decay

The temperature dependence of the Raman peaks is related to the anharmonic interactions involved in the phonon decay process. In this section we present Raman spectra of all the Raman active modes taken at different temperatures. The temperature behavior of the peak linewidths is studied with the model presented in Sec. III A and the decay channels are discussed.

1. The E_2 modes

The E_2^{low} and E_2^{high} phonon modes are the dominant peaks of the first-order InN Raman spectra (see Fig. 2). Despite being modes of the same symmetry, their temperature dependence is remarkably different. While the E_2^{low} frequency and linewidth change only slightly as the temperature is increased, the E_2^{high} Raman peak displays a substantial broadening and downward shift. This different temperature behavior gives indication of the distinct mechanisms taking place in the E_2^{low} and E_2^{high} decay processes.

To resolve the extremely narrow linewidth of the E_2^{low} mode, the high-resolution triple additive configuration of the spectrometer was used. Figure 3(a) shows representative Raman spectra of the E_2^{low} mode in the range of temperatures studied. The intensity of the E_2^{low} Raman peak increases with temperature, as expected from the increase in the occupation factor of such a low-energy phonon. Only a small frequency shift of about 1 cm^{-1} over the whole temperature range is apparent from these spectra.

Because of its low frequency, the E_2^{low} phonon mode cannot decay into lower-energy phonons. As can be seen in Fig. 1(c), the two-phonon sum DOS is very low at frequencies below 150 cm^{-1}. Thus, up-conversion processes in which a higher-energy phonon is created and a second phonon is absorbed are required for the E_2^{low} decay. The role of the up-conversion processes is substantiated by the relatively high two-phonon DOS for phonon differences at the E_2^{low} frequency. By inspection of the phonon dispersion curves

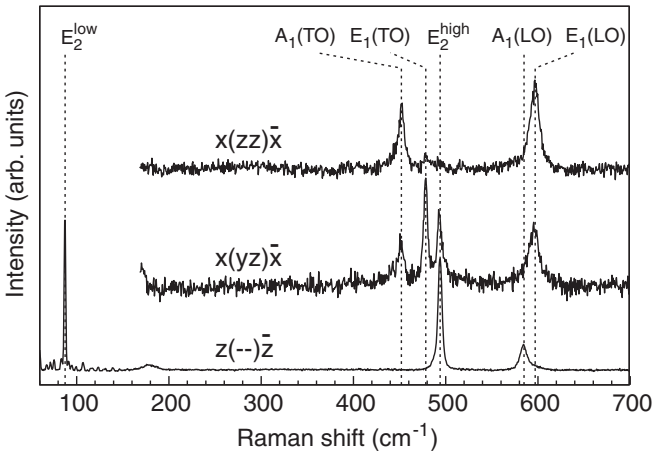

FIG. 2. Room-temperature first-order Raman spectra of InN in the scattering configurations used in this paper.

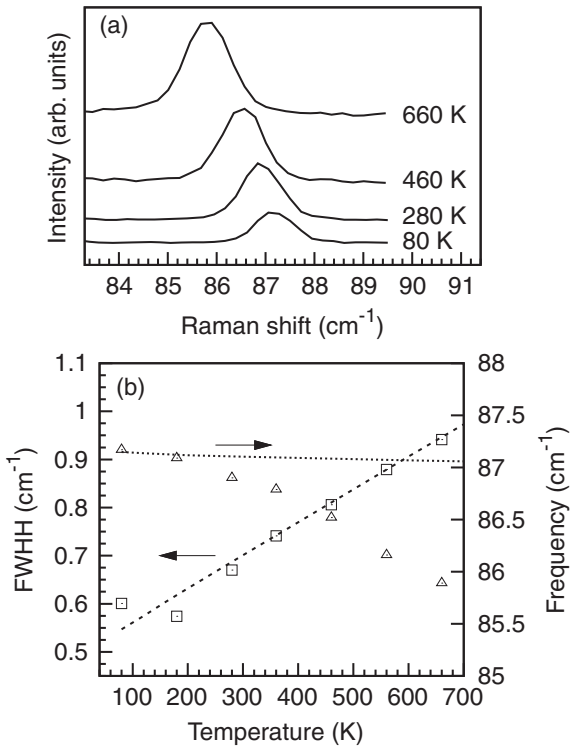

FIG. 3. Temperature dependcence of the E_2^{low} phonon mode. (a) Representative Raman spectra for temperatures in the 80–660 K range. (b) Temperature dependence of the linewidth (squares, left axis) and the frequency (triangles, right axis). The dashed line is a fit of the model discussed to the linewidth data. The dotted line shows the temperature dependence of the frequency given by the model for the same set of parameters.

[Fig. 1(a)] and phonon DOS [Fig. 1(b)], we identify the most likely up-conversion channel as $E_2^{\text{low}} \rightarrow \text{LA}(M)-\text{TA}(M)$, where $\omega(\text{TA}) = 118\ \text{cm}^{-1}$ and $\omega(\text{LA}) = 202\ \text{cm}^{-1}$. Another possible channel that would match the E_2^{low} frequency would be $E_2^{\text{low}} \rightarrow \text{LO}(M)-\text{TO}(M)$, where $\omega(\text{TO}) = 498\ \text{cm}^{-1}$ and $\omega(\text{LO}) = 579\ \text{cm}^{-1}$. However, because of the high energies involved relative to $k_B T$, the Bose–Einstein factors for this channel are very small, and the channel can be neglected.

In Fig. 3(b) we plot the frequency and the FWHM after correcting for instrumental broadening of the E_2^{low} Raman peak as a function of temperature. To analyze the FWHM temperature dependence we have used the anharmonic decay model described in Sec. III A, taking into account only the difference term in Eq. (2). An additive contribution to the phonon linewidth Γ_0 that takes into account the scattering with defects and impurities is included in the model. By fitting Γ_0 and V_3^- to the experimental data we obtain $\Gamma_0 = 0.5\ \text{cm}^{-1}$ and $|V_3^-|^2 = 56\ \text{cm}^{-2}$. As can be seen in Fig. 3(b), the model predicts a linear increase of the FWHM with increasing temperature which is characteristic of the low phonon energies relative to $k_B T$ involved in the decay channel.

Using the anharmonic coupling parameter V_3^- obtained from the FWHM fit, the anharmonic contribution to the temperature dependence of the E_2^{low} frequency has been calculated, and it is also plotted in Fig. 3(b). It is worth noting that the calculations do not predict any measurable frequency shift as temperature is increased. As the InN E_2^{low} mode has a negative Grüneisen parameter (see Table I), the lattice thermal expansion induces an upward frequency shift which nearly compensates for the downward shift that results from the cubic anharmonicity. The experimental data actually show a small frequency downshift (about 1 cm^{-1} over the whole temperature range studied) that can be attributed to deviations in the calculated Grüneisen parameter and/or to a temperature-dependent biaxial strain induced by differential thermal expansion of the sapphire substrate.

In previous studies of the E_2^{high} temperature dependence,[30,31] the experimental data were analyzed using a simplified anharmonic model in which only the variation of the Bose–Einstein coefficients was taken into account. According to the analysis based on that model, it was concluded that the E_2^{high} phonon mode decays through a generic, symmetric four-phonon process and no specific decay channels were identified.[30,31] Here we present a comprehensive study of the E_2^{high} phonon decay using the general model described in Sec. III A, which yields a more realistic description of the E_2^{high} decay processes and gives insight into the most likely decay channels involved.

Representative E_2^{high} spectra in the temperature range studied are displayed in Fig. 4(a). The E_2^{high} Raman peak shows a considerable broadening and downward frequency shift with increasing temperature. As already mentioned in Sec. III B, both the two-phonon sum and difference DOS are very low in the region corresponding to the E_2^{high} frequency ($489\ \text{cm}^{-1}$). This suggests that higher-order processes will be required to explain the strong anharmonicity effects observed in the E_2^{high} Raman peak. Furthermore, the quadratic increase of the linewidth vs. temperature [see Fig. 4(b)] is a clear indication that higher-order processes govern the E_2^{high} phonon decay.[41] Then, four-phonon processes are included in the anharmonicity study of this phonon mode.

As discussed in Sec. III A we assume that the dominant four-phonon processes involve a zone-center phonon and pairs of opposite wavevector phonons at high-symmetry points. By inspection of the phonon dispersion curves and DOS two such decay channels can be identified: (i) $E_2^{\text{high}} \rightarrow E_2^{\text{low}}(\Gamma) + 2\text{TO}(\Gamma - K, M - \Gamma)$ [$\omega(E_2^{\text{low}}) = 84\ \text{cm}^{-1}$, $\omega(\text{TO}) = 202\ \text{cm}^{-1}$], and (ii) $E_2^{\text{high}} \rightarrow E_2^{\text{low}}(\Gamma)+\text{TO}(A-H)-\text{TA}(A-H)$ [$\omega(E_2^{\text{low}}) = 84\ \text{cm}^{-1}$, $\omega(\text{TO}) = 495\ \text{cm}^{-1}$, $\omega(\text{TA}) = 91\ \text{cm}^{-1}$].

Then, the FWHM temperature dependence has been modeled taking into account the cubic contribution [Eq. (2), with $|V_3^+|^2 = |V_3^-|^2$] and the quartic contribution [Eq. (3)]. By fitting $\Gamma(\omega) = \Gamma_0 + \Gamma^{(3)}(\omega) + \Gamma^{(4)}(\omega)$ to the experimental data points we find that the observed temperature dependence of E_2^{high} FWHM is closely matched and we obtain $|V_3^+|^2 = 50\ \text{cm}^{-2}$, $|\tilde{V}_4^+|^2 = 170\ \text{cm}^{-2}$, $|\tilde{V}_4^-|^2 = 34\ \text{cm}^{-2}$, and $\Gamma_0 = 1.9\ \text{cm}^{-1}$. As can be seen in Fig. 4(b) a good fit to the experimental linewidths is obtained over the whole temperature range.

The anharmonic renormalization of the E_2^{high} frequency was calculated with the parameters determined above, and the resulting temperature dependence is also plotted in Fig. 4(b).

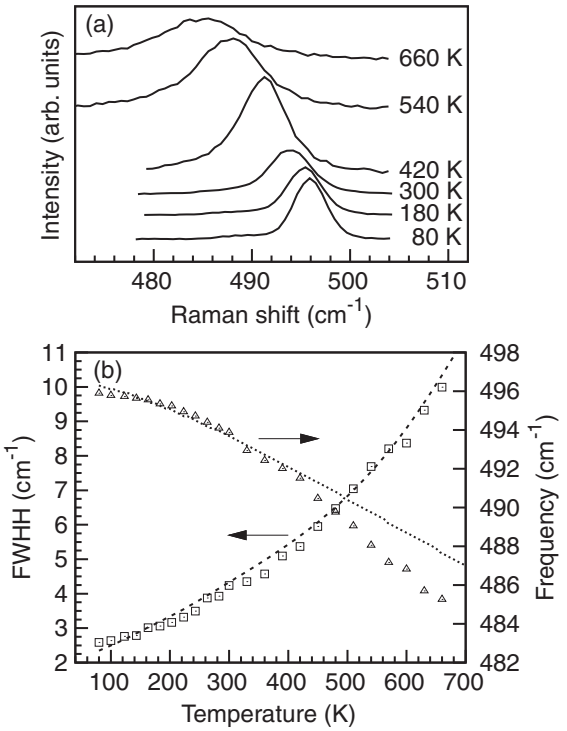

FIG. 4. Temperature dependence of the E_2^{high} phonon mode. (a) Measured Raman spectra for temperatures ranging from 80 to 660 K. (b) Temperature dependence of the linewidth (squares, left axis) and the frequency (triangles, right axis). The dashed line is a fit of the model discussed to the linewidth data. The dotted line shows the temperature dependence of the frequency given by the model for the same set of parameters.

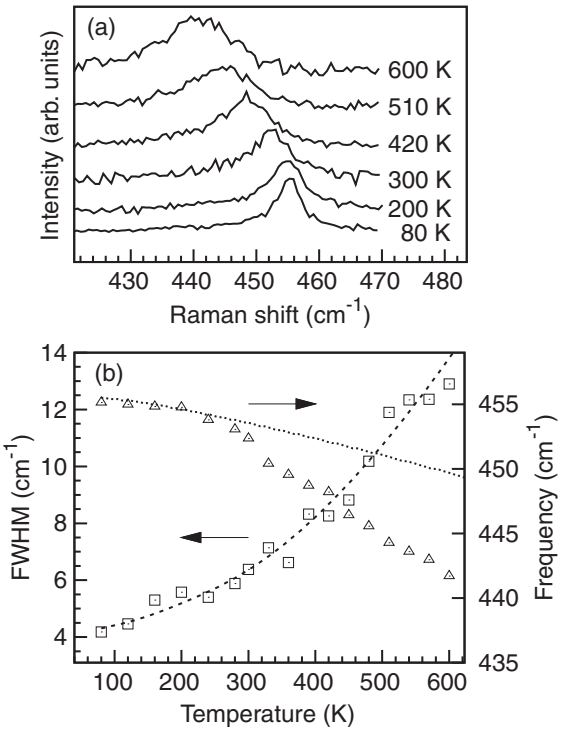

FIG. 5. Temperature dependence of the A_1(TO) phonon mode. (a) Raman peak for temperatures in the 80–600 K range under $x(zz)\bar{x}$ configuration, measured from the m-face sample. (b) Temperature dependence of the linewidth (squares, left axis) and the frequency (triangles, right axis). The dashed line is a fit of the model discussed to the linewidth data. The dotted line shows the temperature dependence of the frequency given by the model for the same set of parameters.

A good agreement is found with the experimental E_2^{high} frequencies obtained from the Raman measurements at low temperature, but a deviation of about 2 cm^{-1} is observed for higher temperatures. This deviation may be attributed to the temperature-dependent biaxial strain induced by differential thermal expansion relative to the buffer layer and substrate.

2. The A_1(TO) and E_1(TO) modes

Figures 5(a) and 6(a) show representative A_1(TO) and E_1(TO) spectra, respectively, which exhibit a significant broadening and downward frequency shift. Owing to the weak signal obtained from the m-face sample at high temperatures, the maximum temperature considered for the anharmonicity study is lower than in the previous section. The A_1(TO) and E_1(TO) phonon modes of InN have similar behavior and similar frequencies, so we can make some common considerations concerning the anharmonic decay of these modes. The inspection of the two-phonon DOS shows that the A_1(TO) and E_1(TO) frequencies lie in a two-phonon-difference DOS plateau, whereas the two-phonon-sum DOS is almost zero in the same region. Thus, up-conversion processes are the only three-phonon mechanisms which can take place in the decay of these modes. Although the A_1(TO) and E_1(TO) phonon modes can decay through several three-phonon mechanisms, the inspection of the calculated phonon dispersion curves and DOS (Fig. 1) allows us to identify the most likely channel as $A_1(\text{TO}) \rightarrow \text{TO}(M)-\text{TA}(M)$ [$\omega(\text{TO}) = 523\,\text{cm}^{-1}$, $\omega(\text{TA}) = 80\,\text{cm}^{-1}$] and $E_1(\text{TO}) \rightarrow \text{LO}(L)-\text{TA}(L)$ [$\omega(\text{LO}) = 581\ \text{cm}^{-1}$, $\omega(\text{TA}) = 106\,\text{cm}^{-1}$], respectively. Furthermore, the linewidth of both the A_1(TO) and E_1(TO) phonon modes exhibits a nonlinear behavior when the temperature increases [Figs. 5(b) and 6(b)], which suggests that four-phonon interactions also have to be included in the study of their respective decay processes. Therefore, the anharmonic decay of these modes is studied by analyzing the temperature dependence of their linewidth, taking into account the cubic and quartic anharmonicity contributions. From the cubic anharmonicity expression [Eq. (2)] we retain only the difference term. The quartic anharmonicity contribution is evaluated in the approximation given by [Eq. (3)], in which the most likely four-phonon mechanisms are also identified from the phonon dispersion curves and DOS.

In the case of the A_1(TO) phonon mode, two four-phonon processes are considered: (i) $A_1(\text{TO}) \rightarrow E_2^{\text{low}}(\Gamma) + \text{LO}(M) - \text{LA}(M)$ [$\omega(E_2^{\text{low}}) = 84\ \text{cm}^{-1}$, $\omega(\text{LO}) = 570\,\text{cm}^{-1}$, $\omega(\text{LA}) = 204\,\text{cm}^{-1}$], and (ii) $A_1(\text{TO}) \rightarrow B^{\text{low}}(\Gamma) + 2\text{TA}(M)$ [$\omega(B^{\text{low}}) = 224\ \text{cm}^{-1}$, $\omega(\text{TA}) = 113\ \text{cm}^{-1}$]. The parameters obtained from the fit are $|V_3^-|^2 = 100\ \text{cm}^{-2}$, $|\tilde{V}_4^{-,(\text{i})}|^2 = 100\ \text{cm}^{-2}$, $|\tilde{V}_4^{+,(\text{ii})}|^2 = 50\ \text{cm}^{-2}$, and $\Gamma_0 = 4\ \text{cm}^{-1}$.

In the case of the E_1(TO) phonon mode, the examination of the PDOS indicates that the most suitable four-phonon processes are (i) $E_1(\text{TO}) \rightarrow E_2^{\text{low}}(\Gamma) + \text{TO}(M) - \text{TA}(M)$ [$\omega(E_2^{\text{low}}) = 84\ \text{cm}^{-1}$, $\omega(\text{TO}) = 541\,\text{cm}^{-1}$, $\omega(\text{TA}) = 150\,\text{cm}^{-1}$], and (ii) $E_1(\text{TO}) \rightarrow B^{\text{low}}(\Gamma) +$

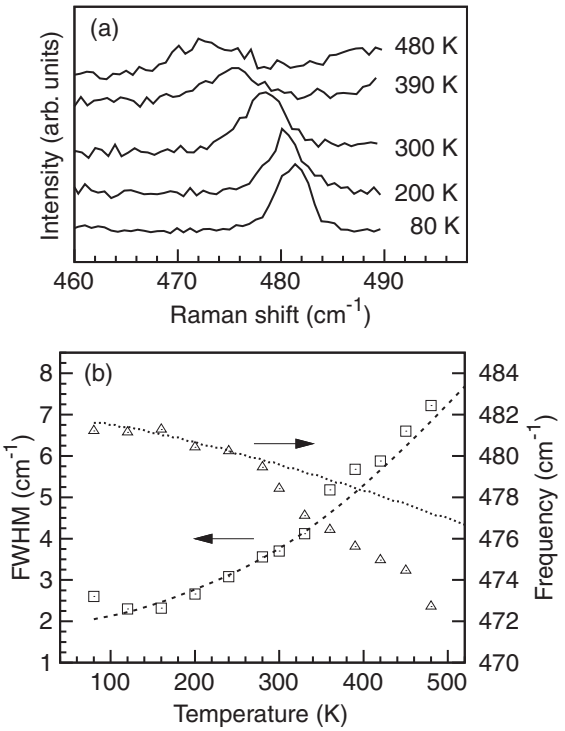

FIG. 6. Temperature dependence of the E_1(TO) phonon mode. (a) Measured Raman spectra for temperatures in the 80-480 K range under $x(zy)\bar{x}$ configuration. (b) Temperature dependence of the linewidth (squares, left axis) and the frequency (triangles, right axis). The dashed line is a fit of the model discussed to the linewidth data. The dotted line shows the temperature dependence of the frequency given by the model for the same set of parameters.

$2\text{TA}(K-M)$ [$\omega(B^{\text{low}}) = 224$ cm^{-1}, $\omega(\text{TA}) = 126$ cm^{-1}]. The parameters given by the resulting fit are $|V_3^-|^2 = 20\,\text{cm}^{-2}$, $|\tilde{V}_4^{-,(\text{i})}|^2 = 39\,\text{cm}^{-2}$, $|\tilde{V}_4^{+,(\text{ii})}|^2 = 60\,\text{cm}^{-2}$, and $\Gamma_0 = 1.9\,\text{cm}^{-1}$. The curves resulting from the fits of the A_1(TO) and the E_1(TO) FWHM are plotted in Figs. 5(b) and 6(b), respectively, and show very good agreement with the measured linewidth temperature dependence of the Raman peak. In both cases, including four-phonon processes has been necessary to properly describe the temperature dependence of the Raman linewidth data.

The anharmonic frequency shift of the A_1(TO) and E_1(TO) modes corresponding to the anharmonic coupling parameters determined from the FWHM fits are also plotted in Figs. 5(b) and 6(b), respectively. In both cases the experimental data show a higher frequency shift when the temperature is increased than expected from the anharmonicity calculations. We suggest the differential thermal expansion of the substrate as the reason for this deviation. Both the A_1(TO) and the E_1(TO) Raman spectra were obtained from an m-face sample grown on (100) γ-$LiAlO_2$. The thermal expansion coefficient along the in-plane (001) direction is $\alpha_c = 14.9 \times 10^{-6}$ Å K^{-1} for γ-$LiAlO_2$,[35] whereas in the case of InN is only $\alpha_c = 2.6 \times 10^{-6}$ Å K^{-1}.[32] As the thermal expansion coefficient of the substrate is much higher than that of the InN, an additional temperature-dependent frequency downshift is expected because of the tensile biaxial strain induced by the differential thermal expansion, which may explain the discrepancy between the calculated and the measured frequency shift in the m-face samples.

3. The A_1(LO) and E_1(LO) modes

Figures 7(a) and 8(a) show, respectively, Raman spectra of the A_1(LO) and E_1(LO) phonon modes recorded at different temperatures. These modes display the strongest downshifts and broadenings of all Raman active modes of InN. According to the calculated phonon dispersion curves and DOS [Fig. (1)] the most likely three-phonon channel can be identified as $A_1(\text{LO}) \rightarrow \text{TO}(A-H)+\text{TA}(A-H)$ [$\omega(\text{TO}) = 500$ cm^{-1}, $\omega(\text{TA}) = 89$ cm^{-1}] and $E_1(\text{LO}) \rightarrow \text{TO}(L)+\text{TA}(L)$ [$\omega(\text{TO}) = 505$ cm^{-1}, $\omega(\text{TA}) = 96$ cm^{-1}], respectively.To fit the FWHM vs. T data obtained from the Raman measurements we have to include in the model the cubic anharmonicity contribution corresponding to phonon sums [Eq. (2)] as well as the quartic contribution [Eq. (3)]. For the latter, we consider the most likely channels to be $A_1(\text{LO}) \rightarrow E_2^{\text{high}}(\Gamma)+\text{LA}(M)-\text{TA}(M)$ [$\omega(E_2^{\text{high}}) = 488.6$ cm^{-1}, $\omega(\text{LA}) = 218$ cm^{-1}, $\omega(\text{TA}) = 118$ cm^{-1}], and $E_1(\text{LO}) \rightarrow E_2^{\text{high}}(\Gamma)+\text{LA}'(M)-\text{TA}'(M)$ [$\omega(E_2^{\text{high}}) = 488.6$ cm^{-1}, $\omega(\text{LA}') = 202$ cm^{-1}, $\omega(\text{TA}') = 85$ cm^{-1}]. The resulting parameters are $|V_3^+|^2 = 600\,\text{cm}^{-2}$, $|\tilde{V}_4^-|^2 = 120\,\text{cm}^{-2}$ and $\Gamma_0 = 2\,\text{cm}^{-1}$ for the A_1(LO) mode and $|V_3^+|^2 = 450\,\text{cm}^{-2}$, $|\tilde{V}_4^-|^2 = 200\,\text{cm}^{-2}$, and $\Gamma_0 = 4.5\,\text{cm}^{-1}$ for the E_1(LO) mode. The anharmonic coupling strength is found to be significantly higher for the A_1(LO) and E_1(LO) modes than for their TO counterparts. The curves corresponding to the results of the FWHM fits are plotted in Figs. 7(b) and 8(b) respectively, and show very good agreement with the experimental points. The obtained parameters indicate that the A_1(LO) and E_1(LO) phonon modes decay mainly by three-phonon mechanisms, but four-phonon interactions have also to be considered to properly describe the linewidth temperature dependence. This is in contrast with previous studies in which, based on a simplified anharmonic model, it was concluded that the A_1(LO) phonon mode decays asymetrically through a three-phonon process into a high-energy and a low-energy phonon.[30,31]

As can be seen in Figs. 7(b) and 8(b), the measured frequency downshift with T is much larger than the anharmonic contribution calculated with the anharmonic coefficients determined above. This suggests that other temperature-dependent mechanisms are affecting the phonon frequencies. In the case of the E_1(LO) mode, which has been measured from the m-face sample, biaxial strain due to thermal differential expansion of the substrate could lower the E_1(LO) frequency at high T, as discussed in the previous section. However, since this effect is expected to yield shifts similar to those observed for the E_1(TO) mode, it cannot fully account for the large frequency shift measured for the E_1(LO) mode. In the case of the A_1(LO) phonon mode, which was measured on the c-face sample, the contribution of the substrate differential expansion is expected to be smaller than for the E_1(LO), since it should be of the same order as in the case of the E_2 modes.

We suggest the temperature dependence of the dielectric constant ϵ_∞ and of the effective transverse charge e_T^*, which results in a temperature dependent TO-LO splitting, may explain the large deviation of the measured LO frequencies

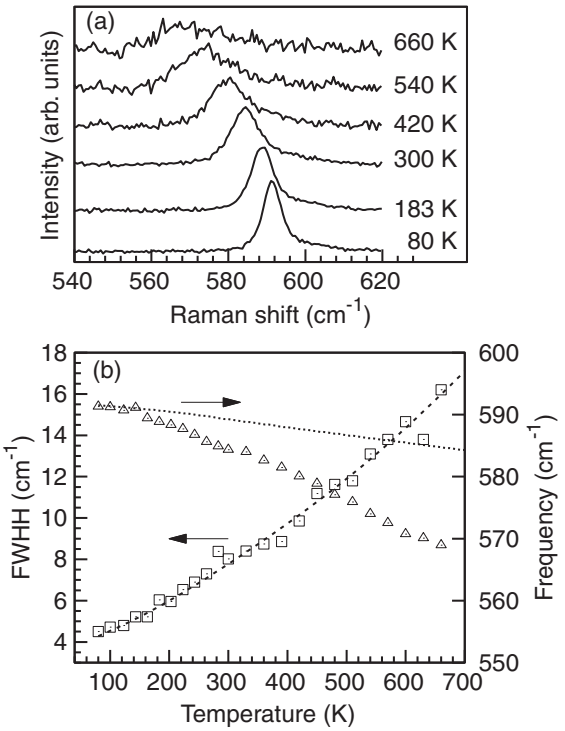

FIG. 7. Temperature dependence of the A_1(LO) phonon mode. (a) Measured Raman spectra for temperatures in the 80–660 K range from the *c*–face sample. (b) Temperature dependence of the linewidth (squares, left axis) and the frequency (triangles, right axis). The dashed line is a fit of the model discussed to the linewidth data. The dotted line shows the temperature dependence of the frequency given by the model for the same set of parameters.

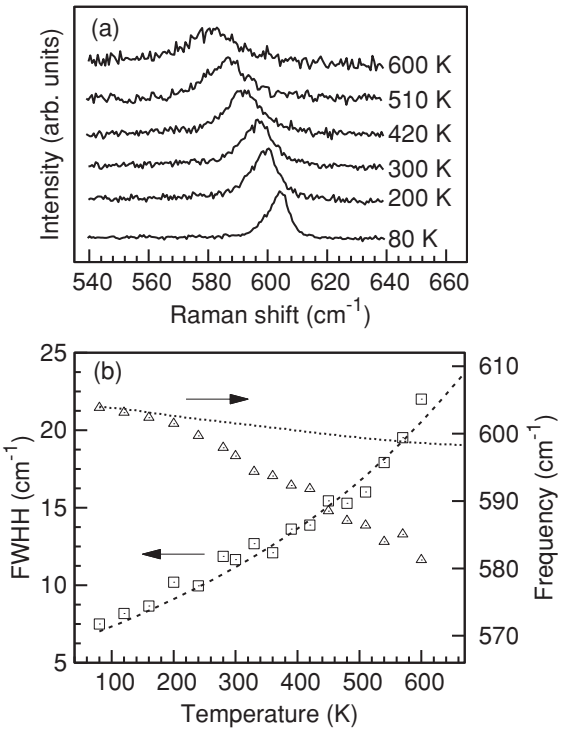

FIG. 8. Temperature dependence of the E_1(LO) phonon mode. (a) Measured Raman spectra from the *m*-face sample in the $x(zz)\bar{x}$ configuration for temperatures in the 80–600 K range. (b) Temperature dependence of the linewidth (squares, left axis) and the frequency (triangles, right axis). The dashed line is a fit of the model discussed to the linewidth data. The dotted line shows the temperature dependence of the frequency given by the model for the same set of parameters.

at high temperature relative to the calculated anharmonic shifts exhibited by both the A_1(LO) and E_1(LO) phonon modes.

C. Phonon lifetimes

The phonon lifetime τ can be evaluated from the Raman linewidth via the energy-time uncertainty relation,

$$\frac{1}{\tau} = \frac{\Gamma}{\hbar}, \tag{8}$$

where Γ is the intrinsic phonon linewidth (after correcting for the spectrometer broadening) and $\hbar$ is Planck's constant. There are two mechanisms which mainly limit phonon lifetime: (i) anharmonic decay of the phonon into other phonons (energy and momentum are conserved) with a characteristic decay time τ_A, and (ii) perturbation of the translational symmetry of the crystal by the presence of impurities and defects, with a characteristic decay time τ_I. Then, the phonon lifetime derived from our Raman measurements can be decomposed as

$$\frac{1}{\tau} = \frac{1}{\tau_A} + \frac{1}{\tau_I}. \tag{9}$$

It is difficult to separate the contribution of both mechanisms, but we can obtain an estimation of the characteristic decay time associated with impurities from the values of the Γ_0 parameter provided by the temperature-dependent FWHM fits. This allows us to provide an estimated value of the phonon lifetime related to impurities for each mode.

The phonon lifetimes at 80 K and room temperature, as well as the estimated impurity-related contribution, are summarized in Table III. The E_2^{low} phonon mode exhibits a remarkably long lifetime (8.8 ps at 80 K). This value is, however, still one order of magnitude lower than that reported for the E_2^{low} in ZnO.[14,60] From our values of τ and τ_I it follows that $\tau_A > \tau_I$, and therefore the impurity effects are the main contribution limiting the lifetime of this mode, which indicates that longer lifetimes can be obtained if sample quality is improved.

Whereas the lifetime we find for the A_1(LO) phonon mode is in good agreement with the values given in Ref. 30, the E_2^{high} lifetime given in Ref. 30 is significantly higher than the value we obtain. As the actual E_2^{high} FWHM reported in Ref. 30 at 80 K is below the quoted spectral slit width, we belive that spectrometer broadening correction may have been overestimated in this case.

The phonon modes measured from the *m*-face sample present a value of the Γ_0 which is, on average, higher than that of the modes measured from the *c*-face sample. This is an indication that the *m*-face sample has a higher defect concentration, as expected from the electrical measurements mentioned in Sec. II. We also note that the defect broadening Γ_0 is significantly higher for the E_2^{high} mode compared with the E_2^{low} mode. We speculate that this may be related to the

TABLE III. Phonon lifetimes of all the studied phonon modes of InN at 80 K and room temperature. The characteristic decay time associated with impurities τ_I is estimated from the background broadening parameter Γ_0 used to fit the FWHM temperature dependence.

	$T = 80$ K		Room temperature			
Phonon mode	Γ (cm^{-1})	τ (10^{-12} s)	Γ (cm^{-1})	τ (10^{-12} s)	Γ_0 (cm^{-1})	τ_I (10^{-12} s)
E_2^{low}	0.6	8.8	0.69	7.7	0.5	10.6
A_1(TO)	4.2	1.3	6.4	0.83	4	1.3
E_1(TO)	2.6	2.0	3.7	1.43	1.9	2.8
E_2^{high}	2.6	2.05	4.2	1.3	1.9	2.8
A_1(LO)	4.5	1.18	8.0	0.66	1.1	4.8
E_1(LO)	7.5	0.71	11.7	0.45	3.1	1.7

presence of N vacancies which affect more strongly the E_2^{high} mode, since it mainly involves N motion.

From Table III we can see that the lifetime of the LO modes is shorter than that of the E_2^{high} and the TO modes. This is probably related to the fact that the latter modes have a restricted space of possible decay routes, as decay channels via pairs of opposite wave-vector phonons are available only for the LO modes. As discussed in Secs. IV B 1 and IV B 2, the E_2 decays through four-phonon processes and for the TO modes the only three-phonon processes correspond to up-conversion processes. Additional decay channels for the LO modes involving the excitation of collective modes of the background electron density may also contribute to shortening the LO phonon lifetime.[11] In previous studies[30] the low-temperature A_1(LO) lifetime was found to increase from 0.7 to 1.3 ps when the layer thickness was increased from 0.25 to 7 μm. For our 550-nm thick InN layer, we obtain an A_1(LO) lifetime of 1.18 ps at 80 K, which is very close to the value reported by Pomeroy *et al.*[30] for a 7-μm-thick layer and demonstrates that long A_1(LO) lifetimes are achieved in high-quality samples with low background electron density and, contrary to previous suggestions,[61] surface roughness does not play a major role in reducing the A_1(LO) lifetime. Although the A_1(LO) lifetime measured in InN is shorter than that reported in GaN (5 ps),[9] it is long enough to give rise to hot-phonon effects in the electron dynamics in InN.[7]

V. SUMMARY AND CONCLUSIONS

In this paper we have presented Raman scattering measurements on wurtzite InN over a temperature range from 80 to 660 K. The linewidth temperature dependence of the Raman active phonons has been studied using an anharmonic model which considers the contribution of three-phonon and four-phonon mechanisms to the decay processes. *Ab initio* calculations of the phonon dispersion curves, PDOS, and two-phonon DOS have been carried out and the obtained results have been used for the implementation of the anharmonic model.

The E_2^{high} phonon mode mainly decays through four-phonon mechanisms, whereas the extremely narrow E_2^{low} mode decays only through up-conversion processes. The decay channels of the transverse optical modes, A_1(TO) and E_1(TO), are found to consist mainly of phonon differences and a small additional contribution of four-phonon mechanisms. The LO modes, A_1(LO) and E_1(LO), mainly decay into a sum of phonons, although the contribution of four-phonon mechanisms is also relevant at high temperatures.

The anharmonic contribution to the frequency downshift has been calculated in all cases from the anharmonic coupling parameters derived from the linewidth analysis. The measured frequency downshift in the case of the E_2 modes is well accounted for by the anharmonic frequency renormalization at low temperatures. In the case of the modes measured from the m-face sample, an extra contibution due to the biaxial strain from the substrate has to be considered. The LO phonons present the highest frequency downshift owing to the temperature dependence of the TO-LO splitting.

Finally, the lifetimes at 80 K and at room temperature have been derived from the measured phonon linewidths. The long-lived E_2^{low} phonon exhibits a lifetime of 8.8 ps at 80 K, which is mainly limited by the impurity broadening. The lifetime of the LO phonons is found to be shorter than that of the E_2^{high} and TO modes. The A_1(LO) lifetime of $\approx$ 1.2 ps at 80 K, although much shorter than that reported for GaN, is long enough to yield a measurable hot phonon effects in InN.

ACKNOWLEDGMENT

This work has been supported by the Spanish Ministry of Science and Innovation under Contract No.MAT2010-16116.

[1] J. Wu, W. Walukiewicz, W. Shan, K. M. Yu, J. W. Ager III, E. E. Haller, H. Lu, and W. J. Schaff, Phys. Rev. B **66**, 201403 (2002).
[2] J. Wu, J. Appl. Phys. **106**, 011101 (2009).
[3] B. Foutz, S. K. O'Leary, M. S. Shur, and L. F. Eastman, J. Appl. Phys. **85**, 11 (1999).
[4] A. Yamamoto, M. R. Islam, T.-T. Kang, and A. Hashimoto, Phys. Status Solidi C **7**, 1307 (2010).
[5] G. D. Chern, E. D. Readinger, H. Shen, M. Wraback, C. S. Gallinat, G. Koblmüller, and J. S. Speck, Appl. Phys. Lett. **89**, 141115 (2006).
[6] F. Chen, A. N. Cartwright, H. Lu, and W. J. Schaff, Appl. Phys. Lett. **83**, 4984 (2003).
[7] D. Zanato, N. Balkan, B. K. Ridley, G. Hill, and W. J. Schaff, Semicond. Sci. Technol. **19**, 1024 (2004).
[8] A. Matulionis, Phys. Status Solidi A **203**, 2313 (2006).
[9] K. T. Tsen, D. K. Ferry, A. Botchkarev, B. Sverdlov, A. Salvador, and H. Morkoc, Appl. Phys. Lett. **72**, 2132 (1998).
[10] K. T. Tsen, J. G. Kiang, D. K. Ferry, H. Lu, W. J. Schaff, H.-W. Lin, and S. Gwo, Appl. Phys. Lett. **90**, 172108 (2007).
[11] G. P. Srivastava, Phys. Rev. B **77**, 155205 (2008).
[12] B. C. Lee, K. W. Kim, M. A. Stroscio, and M. Dutta, Phys. Rev. B **58**, 4860 (1998).
[13] K. T. Delaney, P. Rinke, and C. G. V. de Walle, Appl. Phys. Lett. **94**, 191109 (2009).

[14]C. Aku-Leh, J. Zhao, R. Merlin, J. Menéndez, and M. Cardona, Phys. Rev. B **71**, 205211 (2005).
[15]F. C. Walderman, B. J. Sussman, J. Nunn, V. O. Lorenz, K. C. Lee, K. Surmacz, K. H. Lee, D. Jaksch, I. A. Walmsley, P. Spizziri *et al.*, Phys. Rev. B **78**, 155201 (2008).
[16]J. Menéndez and M. Cardona, Phys. Rev. B **29**, 2051 (1984).
[17]L. Bergman, D. Alexson, P. L. Murphy, R. J. Nemanich, M. Dutta, M. A. Stroscio, C. Balkas, H. Shin, and R. F. Davis, Phys. Rev. B **59**, 12977 (1999).
[18]K. T. Tsen, J. G. Kiang, D. K. Ferry, H. Lu, W. J. Schaff, H.-W. Lin, and S. Gwo, J. Phys. Condens. Matter **19**, 236219 (2007).
[19]J. Serrano, F. J. Manjón, A. H. Romero, F. Widulle, R. Lauck, and M. Cardona, Phys. Rev. Lett. **90**, 055510 (2003).
[20]R. Cuscó, E. Alarcón-Lladó, L. Artús, J. Ibáñez, J. Jiménez, B. Wang, and M. J. Callahan, Phys. Rev. B **75**, 165202 (2007).
[21]M. Kuball, J. M. Hayes, Y. Shi, and J. H. Edgar, Appl. Phys. Lett. **77**, 1958 (2000).
[22]M. S. Liu, L. A. Bursill, S. Prawer, K. W. Nugent, Y. Z. Tong, and G. Y. Zhang, Appl. Phys. Lett. **74**, 3125 (1999).
[23]D. Y. Song, S. A. Nikishin, M. Holtz, V. Soukhoveev, A. Usikov, and V. Dimitriev, J. Appl. Phys. **101**, 053535 (2007).
[24]A. Link, K. Bitzer, W. Limmer, R. Sauer, C. Kirchner, V. Schwegler, M. Kamp, D. G. Ebling, and K. W. Benz, J. Appl. Phys. **86**, 6256 (1999).
[25]R. A. Cowley, Rep. Prog. Phys. **31**, 123 (1968).
[26]H.-J. Kwon, Y.-H. Lee, O. Miki, H. Yamano, and A. Yoshida, Appl. Phys. Lett. **69**, 7 (1996).
[27]V. Y. Davydov, V. V. Emtsev, I. N. Goncharuk, A. N. Smirnov, V. D. Petrikov, V. V. Mamutin, V. A. Vekshin, S. V. Ivanov, M. B. Smirnov, and T. Inushima, Appl. Phys. Lett. **75**, 3297 (1999).
[28]G. Kaczmarczyk, A. Kaschner, S. Reich, A. Hoffmann, C. Thomsen, D. J. As, A. P. Lima, D. Schikora, K. Lischka, R. Averbeck *et al.*, Appl. Phys. Lett. **76**, 2122 (2000).
[29]C. Bungaro, K. Rapcewicz, and J. Bernholc, Phys. Rev. B **61**, 6720 (2000).
[30]J. W. Pomeroy, M. Kuball, J. S. H. Lu, X. Wang, and A. Yoshikawa, Appl. Phys. Lett. **86**, 233501 (2005).
[31]X. D. Pu, J. Chen, W. Z. Shen, H. Ogawa, and Q. X. Guo, J. Appl. Phys. **98**, 033527 (2005).
[32]W. Paszkowicz, Powder Diffr. **14**, 258 (1999).
[33]M. Leszczynski, T. Suski, H. Teisseyre, P. Perlin, I. Grzegory, J. Jun, S. Porowski, and T. D. Moustakas, J. Appl. Phys. **76**, 4909 (1994).
[34]R. R. Reeber and K. Wang, J. Mater. Res. **15**, 40 (2000).
[35]M. M. C. Chow, H. C. Huang, D.-S. Gan, and C. W. C. Hsu, J. Cryst. Growth **291**, 485 (2006).
[36]L. F. J. Piper, T. D. Veal, C. F. McConville, H. Lu, and W. J. Schaff, Appl. Phys. Lett. **88**, 252109 (2006).
[37]R. Cuscó, J. Ibáñez, E. Alarcón-Lladó, L. Artús, T. Yamaguchi, and Y. Nanishi, Phys. Rev. B **79**, 155210 (2009).
[38]H. Lu, W. J. Schaff, L. F. Eastman, J. Wu, W. Walukiewicz, V. Cimalla, and O. Ambacher, Appl. Phys. Lett. **83**, 1136 (2003).
[39]J. J. Olivero and R. L. Longbolhum, J. Quant. Spectrosc. Radiat. Transfer **17**, 233 (1977).
[40]P. G. Klemens, Phys. Rev. **148**, 845 (1966).
[41]M. Balkanski, R. F. Wallis, and E. Haro, Phys. Rev. B **28**, 1928 (1983).
[42]M. S. Liu, L. A. Bursill, S. Prawer, and R. Beserman, Phys. Rev. B **61**, 3391 (2000).
[43]B. K. Ridley, J. Phys. Condens. Matter **8**, L511 (1996).
[44]A. Göbel, T. Ruf, C.-T. Lin, M. Cardona, J.-C. Merle, and M. Joucla, Phys. Rev. B **56**, 210 (1997).
[45]M. Canonico, C. Poweleit, J. Menéndez, A. Debernardi, S. R. Johnson, and Y.-H. Zhang, Phys. Rev. Lett. **88**, 215502 (2002).
[46]J. Serrano, A. H. Romero, F. J. Manjón, R. Lauck, M. Cardona, and A. Rubio, Phys. Rev. B **69**, 094306 (2004).
[47]ABINIT is a common project of the Université Catholique de Louvain, Corning Incorporated, and other contributors [http://www.abinit.org]. X. Gonze, J.-M. Beuken, R. Caracas, F. Detraux, M. Fuchs, G.-M. Rignanese, L. Sindic, M. Verstraete, G. Zerah, F. Jollet *et al.*, Comput. Mater. Sci. **25**, 478 (2002).
[48]A. Debernardi, Phys. Rev. B **57**, 12847 (1998).
[49]W. J. Borer, S. S. Mitra, and K. V. Namjoshi, Solid State Commun. **9**, 1377 (1971).
[50]K. Wang and R. R. Reeber, Appl. Phys. Lett. **79**, 1602 (2001).
[51]S. Goedecker, M. Teter, and J. Hütter, Phys. Rev. B **54**, 1703 (1996).
[52]N. Troullier and J. L. Martins, Phys. Rev. B **43**, 1993 (1991).
[53]M. F. Wu, S. Q. Zhou, A. Vantomme, Y. Huang, H. Wang, and H. Yang, J. Vac. Sci. Technol. A **24**, 275 (2006).
[54]P. Giannozzi, S. de Gironcoli, P. Pavone, and S. Baroni, Phys. Rev. B **43**, 7231 (1991).
[55]X. Gonze and C. Lee, Phys. Rev. B **55**, 10355 (1997).
[56]C. Pinquier, F. Demangeot, J. Frandon, O. Briot, B. Maleyre, S. Ruffenach, B. Gil, J. Pomeroy, M. Kuball, H. Hubel *et al.*, Superlattices Microstruct. **36**, 581 (2004).
[57]J. M. Calleja and M. Cardona, Phys. Rev. B **16**, 3753 (1977).
[58]G. Kaczmarczyk, A. Kaschner, S. Reigh, A. Hoffmann, C. Thomson, D. J. As, A. P. Lima, D. Schikora, K. Lischka, R. Averbeck *et al.*, Appl. Phys. Lett. **76**, 2122 (2000).
[59]V. Y. Davydov, A. A. Klochikhin, A. N. Smirnov, I. Y. Strashkova, A. S. Krylov, H. Lu, W. J. Schaff, H.-M. Lee, Y.-L. Hong, and S. Gwo, Phys. Rev. B **80**, 081204 (2009).
[60]M. Millot, R. Tena-Zaera, V. Munoz-Sanjose, J.-M. Broto, and J. Gonzalez, Appl. Phys. Lett. **96**, 152103 (2010).
[61]G. P. Srivastava, J. Phys. Condens. Matter **21**, 174205 (2009).